Chapter 5. Preliminary Visualizations[3]

This list of characteristic multiplicity trends given at the end of the previous chapter is already extensive, but a major deficiency is the fact that all these trends are bed-scale and it is not possible to extract the localized characteristics from them. Additional insights into the distribution of liquid and gas at the local (pore) scale is necessary in order to discern the fundamental mechanism responsible for the multiplicity behaviour. The next two chapters addresses the cluster-of-particles (pore) scale characteristics of hydrodynamic multiplicity (it is Part 2 of the Additional Experimental Insights block in Figure 1). The technique by which this is accomplished is X-ray radio-imaging, of which two variants are employed: temporal radiography (2D) and 3D tomography. Here again, the objective is to identify the nature of hydrodynamic multiplicity at a smaller scale through the extension of the characteristic trends list, i.e. Objective 2 as identified in Chapter 3. In Chapter 7, these insights lead to the proposal of a multiplicity mechanism.

5.1 Background

The main visualization techniques used to study the micro-scale characteristics of trickle flow are colorimetry and non-intrusive imaging (including radiography and computed tomography). In recent years, both techniques have provided insights into the localized behaviour of trickle flow at the cluster-of-particles scale (Lazzaroni et al., 1988, 1989, Ravindra et al., 1997b, Van Houwelingen et al., 2006, Lutran et al., 1991, Toye et al., 1998, Mantle et al., 2001, Sederman & Gladden, 2001, Boyer & Fanget, 2002, Marchot et al., 2001, Anadon et al., 2005, Gladden et al., 2003a, Kantzas, 1994, Reinecke & Mewes,

[3] The work reported in this Chapter was published in Chemical Engineering Journal, Vol. 132, pg 47-59, 2007.

1996, Schmit, et al., 2000, Yin et al., 2002, Gladden et al., 2003b, Basavaraj et al., 2005). In particular, the structure of packed beds and the distribution of the fluid phases in these beds on various scales and under differing circumstances have been given considerable attention. Brief overviews follow.

The colorimetric technique involves colouring the catalyst particles at the locations where the liquid is in contact with the particle surface. The flow is brought to steady state before the feed is switched to a dye solution for either 5 or 20 minutes (Lazzaroni et al., 1988, Ravindra et al., 1997b). The wetting efficiency is calculated directly from the (partially) coloured particles, while the liquid distribution can be inferred from such data (Van Houwelingen et al., 2006). The validity of the technique is dependent upon the assumption that the liquid distribution remains stable throughout the period of dye irrigation. Any flow path deviations during this time will result in non-uniformly coloured particles and probably an over-estimation of the wetting efficiency and the flow uniformity. A further drawback of this method is its intrusive nature. The feed properties are changed by the dye and there are flow rate disturbances that influence the flow stability (Gladden et al., 2003a) and potentially the liquid distribution.

Radiography involves subjecting the trickle bed to some form of radiation (γ-, X- or neutron) and then recording the interaction between the different phases and the radiation (usually in the form of an intensity image). The technique relies on the fact that the different phases attenuate (absorb) the radiation to varying degrees. In computed tomography (CT), the bed is subjected to the radiation at several angles of rotation. From these images a three-dimensional reconstruction of the entire volume under consideration can be made. CT has emerged as a valuable tool for the non-invasive imaging of opaque systems in the chemical and process industries (Chaouki et al., 1997). In terms of trickle flow CT, the liquid distribution has been successfully investigated (for selected conditions) by several authors (Lutran et al., 1991, Toye et al., 1998, Sederman & Gladden, 2001, Gladden et al., 2003a, Kantzas, 1994, Reinecke & Mewes, 1996, Schmit,

et al., 2000, Yin et al., 2002 and Gladden et al., 2003b). However, most of these reports have been mainly concerned with proving the utility of the technique and only to a lesser degree with using the technique to investigate the underlying physical phenomena. CT investigations also assume that the flow remains stable during the acquisition of the images required for the volume reconstruction. These acquisition times can be very short (milliseconds) if one is prepared to accept either relatively poor spatial resolution (millimetres, MRI) or reconstruction artefacts in the final volume image (for example "streak lines" in X-ray tomography). For a greater resolution MRI image of a dry bed (micrometers), Anadon et al. (2005) used an acquisition time of 11.5 hours, but they do not report such high resolution images for trickle flow conditions. Gladden et al. (2003a) conducted a stability analysis of trickle flow using 2D images with acquisition times of 30 seconds per image and an in-plane resolution of 352 μm per pixel. For radiation-based CT, longer acquisition times will be required for larger diameter beds. A summary of CT and radiography investigations (with pertinent experimental conditions) into the trickle flow regime is given in Table 14. The trade-off between spatial resolution and acquisition time means that sufficiently high frequency flow path deviations can either not be detected (for the radiation-based CT. i.e. long acquisition times) or cannot be detected with a resolution smaller than a few millimetres per voxel (for example MRI). Note that there are three beam geometries for X- or γ-ray tomography. If fan beam geometry is used, it is possible to acquire rapid 2D cross-sectional images, but the question remains whether these are representative of the entire bed. Parallel beam geometry allows relatively rapid acquisition of radiographs, but no geometric enlargement of the sample. Cone beam geometry allows rapid radiograph acquisition as well as geometric enlargement of the sample, but introduces an element of inaccuracy called unsharpness. Some representative results form literature are reproduced in Figure 29.

Table 14. Trickle flow CT and radiation studies in literature

Reference	Type	Bed size (cm) D x H	Packing	Modes	Spatial resolution (μm)	TSS (min)	Acquisition time (s)
Lutran et al. (1991)	X-ray	6.03 x 19.05	Glass spheres	NPW, Kan-Liquid	500	n/r	26 (2D)
Kantzas (1994)	X-Ray	4.5 x 45	Glass spheres	NPW	400 x 400 x 3000	n/r	450 (3D*)
Reinecke & Mewes (1996)	Capacitance	12 x 200	Celcore spheres	N/A	6000-12000	n/r	0.01 (2D)
Toye et al. (1998)#	X-ray	80 x 200	Polypropylene wheels	n/r	880	n/r	150 (3D*)
Schmidt et al. (2000)	X-ray	20 x 25	Ceramic spheres	NPW, pre-wetted	400	n/r	900 (3D*)
Mantle et al. (2001)	MRI	4 x 55	Extrudate, spheres	NPW	313	160	n/r
Sederman & Gladden (2001)	MRI	4 x 50	Glass ballotini	NPW, Levec	328	n/r	21600 (3D*)180 (2D)
Marchot et al. (2001)#	X-ray	60 x 200	Polypropylene packing	n/r	1000	n/r	160 (2D)
Yin et al. (2002)	γ-ray	60 x 60	Pall rings	n/r	n/r	n/r	n/r
Boyer & Fanget (2002)	γ-ray	60 x n/r	Alumina extrudate	n/r	n/r	n/r	2700 (2D)
Gladden et al. (2003a)	MRI	70 x 4.5	Porous cyllinders	n/r	352	n/r	30 (2D)
Gladden et al. (2003b)	MRI	4 x 50	Alumina extrudate	Wetted	156	n/r	1500 (2D)
Basavaraj & Gupta (2004), Basavaraj et al. (2005)	X-ray	17 x 6 (rectangular) 75 (height)	Polystyrene spheres	NPW	757 x 757 x 60000	15	900 (2D)
Anadon et al. (2005)	MRI	4.3 x 70	Porous extrudate	Levec	3750 x 3750 x 1870 175 x 175 x 175	n/r	0.28 (3D*) 41400 (3D*)

n/r: not reported, TSS: Time to reach Steady State, NPW: Non-pre-wetted, * 3D images are obtained by stacking 2D images (obtained at several axial locations) on top of one another, # These authors investigated structured packings.

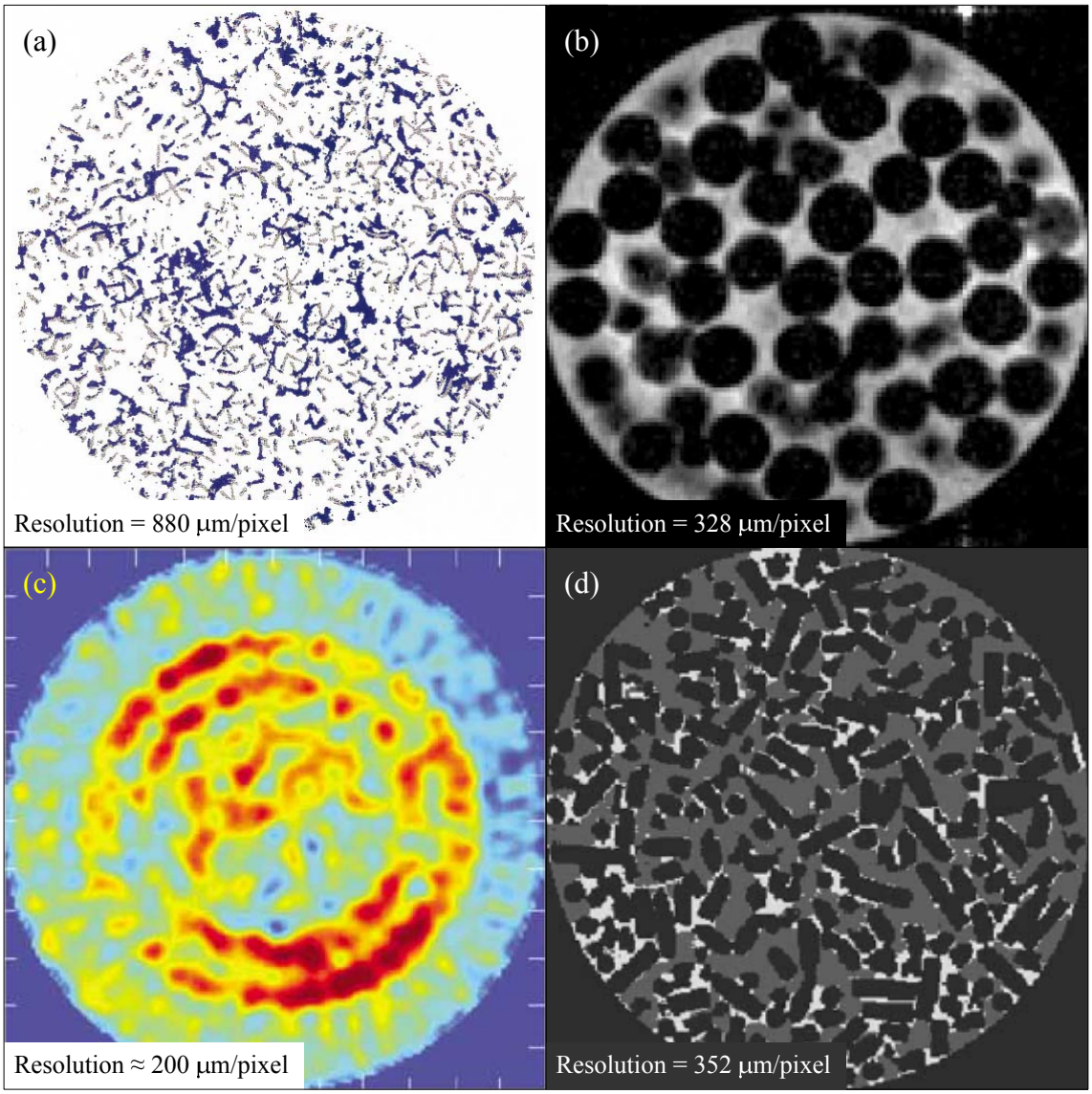

Figure 28. CT results from earlier investigators - representative of various techniques, (a) γ-ray: Toye et al. (1998) – liquid in blue, solid in grey, (b) MRI: Sederman & Gladden (2001) – solid in black, liquid in white, (c) X-ray: Boyer & Fanget (2002) – liquid saturation intensity image, (d) Processed MRI: Gladden et al. (2003a) – solid in black, liquid in white. Additional detail in Table 14. Also see Figure 8b for a representative capacitance tomography image.

5.2 Introduction

The aim of any (including the present one) particle-scale CT investigation is to establish the spatial locations and temporal behaviour of the three phases. It is evident from the preceding discussion that there is a need for determining the stability of trickle flow with high spatial and temporal resolutions. However, the objectives of both high spatial and high temporal resolution are mutually exclusively. For this reason, *radiography* is used here to obtain high temporal resolution 2D images of a section of the bed, while *tomography* is used to obtain high spatial resolution 3D images of the bed. The high temporal resolution 2D images is necessary because a proper interpretation of computed tomographical reconstructions is dependent upon the knowledge of whether or not the volume images are time-averaged representations of liquid and gas distributions or in fact a stable phase distribution configuration. The high spatial resolution 3D images then form the basis of an investigation into the local flow structures in the various multiplicity modes.

In the first part of this study, cone beam X-ray *radiography* is used to study the temporal stability of trickle flow. Radiography is better suited to the investigation of liquid saturation in porous media because it does not require exact phase-border distinction in order to attain phase saturations. X-ray radiography has been used successfully to study both liquid saturation and distribution in trickle flow packed beds (Basavaraj & Gupta, 2004, Basavaraj et al., 2005). In simple terms the focus here is to:

- Compare radiography and gravimetry as tools for a hydrodynamic investigation of trickle flow.
- Visualize the flow patterns encountered in different hydrodynamic states. The radiographic technique employed here provides visualisations of the overall liquid distribution in the bed for different fluid velocities and pre-wetting histories, the importance of which has been emphasized by Sederman & Gladden (2001),

Basavaraj & Gunjal (2004), Basavaraj et al. (2005), Marcandelli et al. (2000), Wang et al. (1995), Hoek et al. (1986) and Toye et al. (1995).

- Determine whether trickle flow is stable locally in the bed. In particular, to illustrate the usefulness of rapidly acquired radiographs to analyse the liquid distribution and its dynamic behaviour. There is some discrepancy as to the time it takes (from start-up) to reach steady state. This start-up time appears to vary considerably depending on the pre-wetting procedure (Ravindra et al., 1997b). The start-up dynamics are therefore also investigated.
- Establish whether the flow distributions and liquid saturations are reproducible provided that the same pre-wetting procedure was followed.

This first part of the radio-imaging (radiography) illustrates how a relatively simple technique can provide new insights into trickle flow phenomena. X-ray radiography has the potential to be scaled up to larger applications with relative ease (Boyer & Fanget, 2002), although the presence of steel reactor walls in industry diminishes this scaling ability.

The second part of the radio-imaging study is to obtain 3D *computed tomographic* images of the various hydrodynamic modes. These images are to provide the experimental basis for a pore scale evaluation of hydrodynamic multiplicity. One objective of such a highly detailed visualization is to obtain the interfacial areas (gas-liquid, liquid-solid and gas-solid), since these areas impact the external mass transfer (Wu et al., 1996), the particle effectiveness (Dudukovic, 1977), the residence time distribution characteristics (Iliuta et al., 1999) and the hydrodynamics in general (Pironti et al, 1998). This objective requires each phase to be properly distinguished in the processed tomograph. For CT studies of high resolution (where individual particles can be observed), the state-of-art method of distinguishing phases is by the method of thresholding (Sederman & Gladden, 2001, Gladden et al., 2003, Toye et al., 1998), whereby a range of image intensities is assigned to each phase. Section 5.4.2 will show the inadequacy of the thresholding technique for the present X-ray CT data.

5.3 Experimental

Radiograph Acquisition

A comprehensive description of the experimental facility as pertains to the acquisition of radiographs is given elsewhere (De Beer, 2005). Figure 29 is a schematic of the setup. The 40 mm (inner diameter) polypropylene column is mounted on a stand. The column is packed with spherical porous γ-alumina catalyst particles of diameter 2.5 mm. Air and water (atmospheric conditions) at controlled flow rates are fed co-currently downward into the bed. These fluids are used for ease of implementation and are the most common fluids found in the trickle bed literature. Experimental gas and liquid flow rates were chosen to represent a wide range of conditions within the trickle flow regime. Liquid superficial velocity varied from 1.3 to 8.0 mm/s and gas velocity from 0 to 16 cm/s. The liquid is distributed uniformly at the top of the bed through 16 equally sized and equally spaced holes; resulting in a drip point density in excess of 10 000 points per square meter. This ensures that the liquid distribution in the bed is independent of the distributor (Burghardt et al., 1995). A uniform initial distribution has been shown to be crucial to achieving proper liquid distribution inside the bed (Ravindra et al., 1997b). The gas enters the bed through a separate ¼" tube located in the centre of the distributor head. For the pre-wetted modes, the bed was flooded for 5 hours prior to experimentation to ensure complete internal saturation of the catalyst spheres (Van der Merwe et al., 2006).

Experimental considerations with regards to the acquisition of X-ray radiographs are the amplitude of the X-ray source, the focal point size, the source-detector distance and the presence of inorganic species in the liquid phase (Toye et al., 1998, Basavaraj & Gupta, 2004, Toye et al., 1995). Extensive testing during the course of this investigation revealed that the experimental conditions listed in Table 15 yield satisfactory results. Note that adequate phase distinction was achieved without the need to add $BaCl_2$. This ensures that the liquid properties were not changed from that of water, reduces beam hardening and reduces deviations from the Beer-Lambert Law (as discussed later).

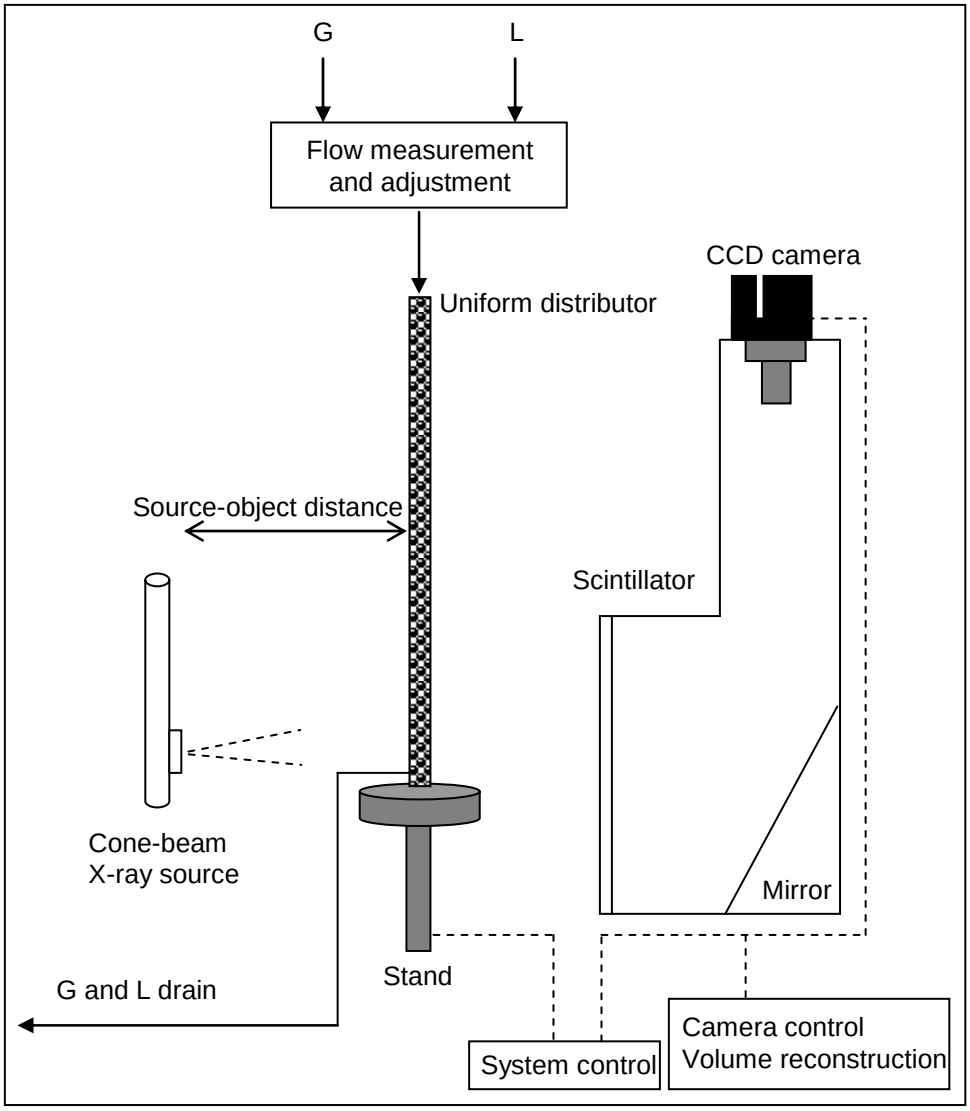

Figure 29. Experimental setup for radio-imaging study

Using these settings, a radiograph of 61 mm of the bed was obtained. The top of the radiographed section was located 539 mm below the top of the bed. This was done specifically to avoid the calming zone at the top of the bed where the liquid distribution is not representative of the entire bed (Gianetto & Specchia, 1992).

Table 15. Experimental parameters for radiography study

X-ray source	Tungsten filament
X-ray amplitude	100 keV (at 6 mA)
Packing	2.5 mm γ-alumina spheres (porous)
Packing height	900 mm
Exposure time	1.5 seconds per radiograph
Delay time (between successive acquisitions)	Approximately 0.5 seconds
Image size (binning)	512 X 512 pixels (2)
Spatial resolution	120 μm/pixel (approximately)
Focal point opening	1 mm
Source object distance (SOD)	610 mm

As in Basavaraj & Gupta (2004), the beam hardening effect is minimized by two measures:

- A low inorganic concentration (in the present study no salt was added to the liquid).
- A hardware filter (in the present study the 5 mm polyethylene column walls acted as a filter for the incoming X-rays).

Representative radiographs are shown in Figure 30. These images were filtered using a 3 × 3 low pass filter in order to remove experimental noise (white spots). In Figure 30a, the column had not been placed in the X-ray beam. The cone beam geometry is evident from the fact that the image intensity is higher in the centre of the image and decreases towards the sides. Figure 30b is the radiograph of the column packed with dry particles. Note that the X-rays traverse the entire diameter (50 mm) of the column only in the centre of the image. As one moves away from the central vertical axis, the intensity increases because the X-rays pass through less material (because of the cylindrical shape of the column) and are therefore not as severely attenuated. The reduction in intensity in the image is related to the thickness of material transverse to the viewing plane. Figure

30c is the same column after the introduction of liquid (Non-pre-wetted mode). The darkening of the image is indicative of the beam being attenuated by the water in the bed. Similarly, radiographs of a pre-wetted and drained bed (no flow) and a bed in the different pre-wetting modes were obtained once the flow had stabilized. There is a geometrical error in these radiographs that stem from the cone geometry of the X-ray beam. X-rays travelling to the top (and bottom) of the image section has a slightly longer path length (and therefore diverges more than those travelling in the plane of the focal point). This results in the top (and bottom) of the image appearing slightly larger than the middle. In the present investigation, this error is negligible because the source-object distance greatly exceeds the size of the sample. The apparent size of the top (and bottom) of the column is approximately 0.5% larger than the apparent size of the middle.

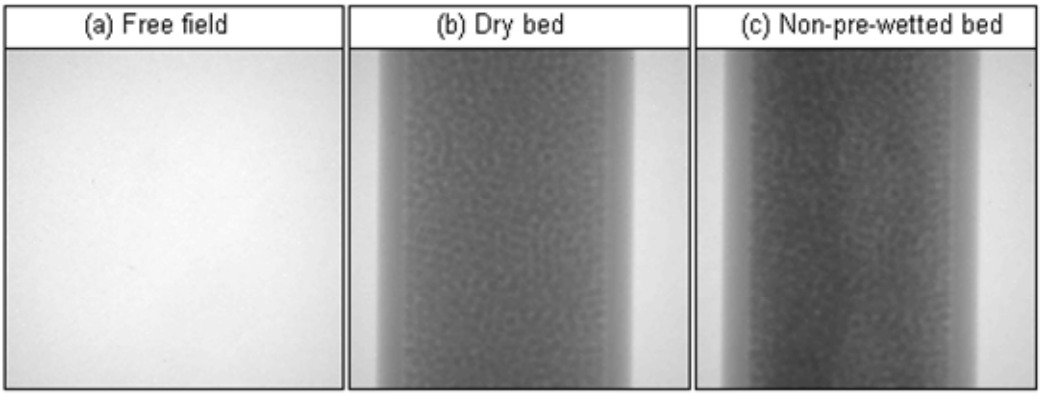

Figure 30. A selection of radiographs

Experimental: Tomography

With a few modifications, the experimental setup can be used to obtain sufficient data for a tomographic investigation. The column is mounted on a computer controlled rotating desk. Two-dimensional radiographs are taken at 1 degree intervals for a full 360 degree rotation. The distributor rotates with the column, thereby ensuring that the top-of-bed distribution is not affected by the rotation. The rotational acceleration is set at a very low value to curb the effects of any centrifugal forces acting on the liquid. For high definition radiographs, utilising the full 16 bit dynamic range of the CCD camera, the total

acquisition time is 16 minutes for the whole volume. The data acquisition frequency therefore is 0.38 images/s, meaning that each radiograph takes 2.6 s to acquire (1.5 s exposure time and 1.1 s to rotate 1 degree). The source-object distance remains at 610 mm, allowing the same geometric enlargement that proved useful in the radiographic imaging. A height of 61 mm of the bed located 539 mm from the top of the bed was imaged. This is in order to avoid the "calming zone" located in the top part of the bed and ensures that the flow pattern is well-established in the imaged section. The bed and operating conditions were the same as in the radiographic study. A set of radiographs was also taken for a drained bed (no liquid flow) to provide a reference for the liquid flow experiments. Preliminary investigations indicated that the Non-pre-wetted mode flow pattern takes at least 8 hours to stabilize (because of the slow internal saturation of the catalyst particles). For this reason, experimental constraints unfortunately dictated that the Non-pre-wetted mode could not be investigated to the same degree as the pre-wetted modes. Tomographic reconstruction is discussed at the end of this chapter.

5.4 Results

5.4.1 Two Dimensional Radiographs

This section is concerned only with the result of the first part of this radio-imaging study, namely radiography.

Radiograph Processing

The intensity of the attenuated image (I) relates to the intensity of a free field image (I_0) according to the Beer-Lambert Law (Toye et al., 1998, Basavaraj et al., 2005):

$$I = I_0 e^{-Ex} \tag{14}$$

Here x is the thickness of the attenuating material and E is the attenuation coefficient (assumed to be independent of x). For a given fluid, E is a function of the intensity of the

X-ray source. At 100 keV its value is 17.07 per meter for water (NIST database). Several processing combinations are possible. Using Figure 30(a) as the free field image (I_0) and Figure 30(b) as the intensity image (I), the solids content in the bed is isolated. Alternatively, setting Figure 30(b) as I_0 and Figure 30(c) as I, the water content in the bed at the time of acquisition is obtained. This however, includes the internal holdup. For pre-wetted beds, the pre-wetted and drained bed is set as I_0 and the irrigated bed as I, yielding the dynamic (more accurately the free-draining) holdup in the bed during operation at the time of acquisition. An example of a Levec mode of operation is shown in Figure 31a. Here, the (dark) intensity of the image is proportional to the thickness of water transverse to the viewing plane. Since the exposure time for such an image is equal to 1.5 seconds, the image actually shows the average water thicknesses in the preceding 1.5 seconds. However, for practical purposes it can be thought of as a snapshot of the liquid in the bed at the time of acquisition.

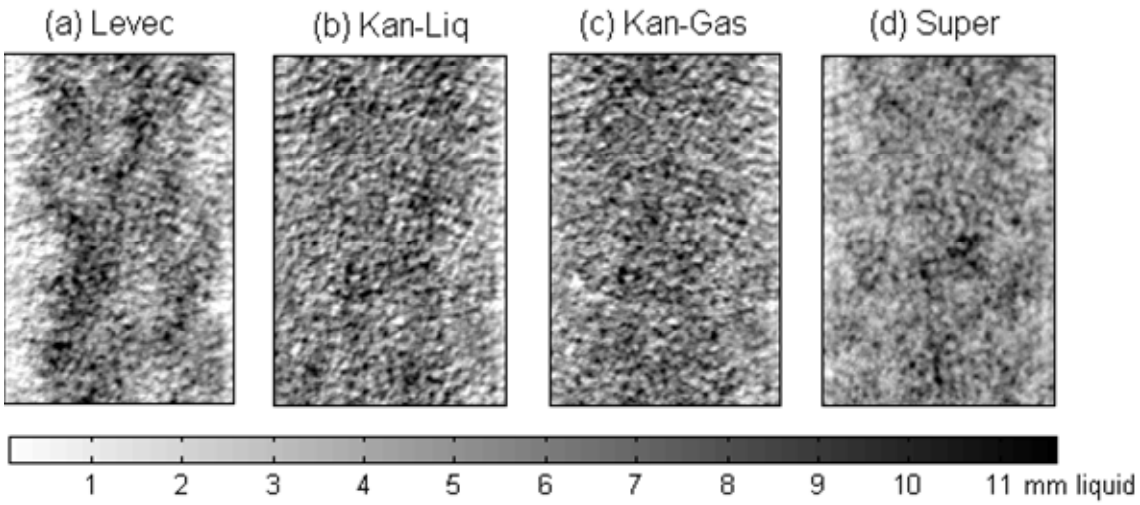

Figure 31. Liquid distribution in the various pre-wetting modes (u_L = 8 mm/s, u_G = 16 cm/s).

Images similar to that shown in Figure 31 were generated for all times (at intervals of 2 seconds), fluid velocities and operating modes. They are used to characterise the stability and uniformity of the flow. Note that any changes in the total amount of liquid in the column or in the distribution of the liquid in the column will register on these images. To

re-iterate, the dark intensity in Figure 31 is the thickness of liquid transverse to the viewing plane. It represents the entire bed and not just the wall flow or a vertical slice of the bed as one would get from a tomographical reconstruction (as originally reported in Lutran et al., 1991).

Liquid Saturation from Radiographs

The liquid saturation (holdup divided by the external porosity) in the field of view of the radiograph is determined from images analogous to those in Figure 31 by summation of the water thickness at each location, i.e.:

$$\text{Dynamic saturation} = \frac{\sum_{\text{all pixels}} x_i . \Delta s^2}{V_{\text{section}} \varepsilon} \qquad (15)$$

The saturation obtained through this radiographic technique may be inaccurate because of:

- The presence of several processing steps (in arriving at Figure 31 and in particular the assumption of a constant attenuation coefficient (E). Improved saturation values can be obtained through a calibration technique (Basavaraj et al., 2005), but the subsequent qualitative investigations into flow stability are not expected to be affected by assuming E to be constant).
- The liquid saturation is only applicable to a section of 61 mm of a 900 mm bed.
- Any high frequency oscillations that occur within the 1.5 seconds of exposure time will register as averaged intensity values.

With regards to liquid distribution, the draw-back of radiography (as opposed to tomography) is evident from equation 14. While the amount (thickness, x) of the liquid in the direction transverse to the image can be obtained (by solving for x in equation 14), all the information on how the liquid is distributed in that direction is lost. Nevertheless, the different flow patterns can still be distinguished (compare Figure 31a to Figure 31b-d). Note also, that any flow fluctuation will be registered as an increase (darkening -

increased saturation) or decrease (lighting – decreased saturation) in the intensity at a location.

Gravimetric Saturation Determination

It is imperative to compare the radiographic interpretation presented here to gravimetric saturation measurements. Since there is a considerable scatter in liquid saturation measurements in literature due to system and operating differences, liquid saturation was measured under conditions similar to those under which the radiographs were taken. Due to practical constraints, the liquid saturation measurement was not done during the actual radiography experiment. Instead, the setup was moved to another location where the column was mounted on an Ohaus Pro 22001 balance that is capable of registering intervals of 0.1 gram in mass. Identical operating procedures were followed for the radiographic and gravimetric experiments. The procedure for determining liquid saturation by gravimetric means involves subtracting the weight of the drained bed from an irrigated bed and is discussed in detail elsewhere (Nemec et al., 2001). Gravimetric saturation measurements were found to be satisfactorily reproducible. Unfortunately, the bed had to be re-packed between the two sets of experiments. However, the bed porosity was found to be very reproducible with re-packing (a value of 0.41 is used throughout this study). Additionally, it was necessary to correct the measurements for significant hysteresis in the amount of water retained in the distributor. In order to properly evaluate the temporal evolution of the liquid saturation, the weight of liquid present in the bed was recorded every second from start-up to steady state (and beyond) for each mode of operation.

Possible inaccuracies in the gravimetric method of holdup determination described here are:

- End effects (including the liquid in the distributor and retained on top of the sieve at the bottom of the bed).

- The gravimetrically determined liquid saturation is a bed-averaged value and therefore includes the non-representative calming zone holdup that may well encompass the first 200 mm of the bed (Gianetto & Specchia, 1992).

The gravimetric liquid saturation measurements serve as a check of the radiographic technique employed here. One would expect the two methods to give similar liquid saturation values at steady state. A selection of results is shown in Figure 32a to Figure 32c. Note that both techniques indicate that liquid saturation increases with liquid flux (Figure 32a to Figure 32b) and decreases with gas flux (Figure 32c). Figure 32d is a parity plot of the liquid saturation at all fluid velocities and all pre-wetting modes as determined by the radiographic and gravimetric techniques. An average absolute relative error (AARE) of 5.5 % indicates that there is excellent agreement between the two techniques, especially considering that a constant attenuation coefficient was used.

Liquid Configuration Variation with Fluid Fluxes

The radiographic technique is suitable for a visualisation of the liquid flow pattern. Figure 33 shows processed radiographs of the bed at steady state for different liquid and gas fluxes. Note that the higher fluxes reported do not imply that the bed was operated at the low flux and that the flux was then increased. Instead, for the Levec mode, the bed was pre-wetted and drained and then the operating fluxes were introduced. If a higher operating value was required, the whole procedure was repeated. For the Kan-Liquid mode the operating fluxes were set, the liquid flow was increased and then decreased to the operating value – again repeating the whole procedure if higher fluxes were required. Similarly, the Super bed was flooded between flow rate changes and the Kan-Gas bed was pulsed (with increased gas flow) between flow rate changes (their results were similar to the Kan-Liquid mode and are not shown). Examination of Figure 33a suggests that in the Levec mode the liquid is improperly distributed through the volume (areas of dark and light) while in the Kan-Liquid mode the liquid is relatively uniformly distributed.

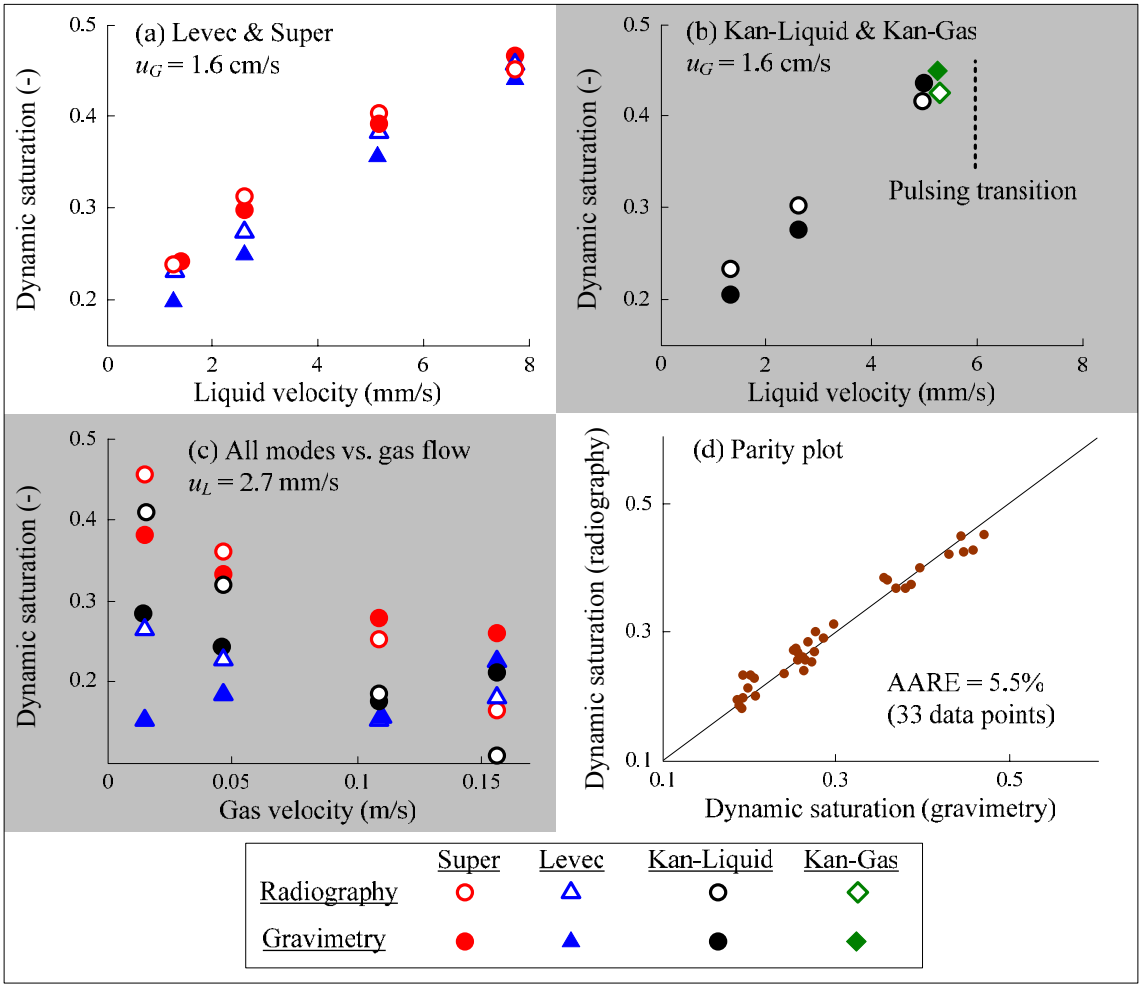

Figure 32. Gravimetric and radiographic saturation comparisons

Moreover, the improper distribution in the Levec mode persists at high liquid velocities. Finally, it appears as though the there are completely dry zones at the low u_L (see for example the lower left corner of the image). Although there is still improper distribution at high u_L, the completely dry zone is absent. This is in agreement with Sederman & Gladden (2001) who reported that there is new rivulet creation as u_L is increased up to 2 mm/s, as well as Van der Merwe & Nicol (2005) and Van Houwelingen et al. (2006) who report completely dry zones at low u_L. From Figure 33b it is not clear what the effect of gas flow is on the liquid morphology. It is apparent however, that the improper liquid distribution in the Levec mode persists at high gas velocity and even appears to increase as a result of the higher gas flux. This is contrary to the expectation that high gas fluxes

will serve to spread the liquid more evenly over the packing. Unexpectedly, there are several dark spots (local volumes of high liquid saturation) in the Kan-Liquid mode at high u_G that are not as apparent at lower u_G. Here the gas may indeed have the expected effect of increasing the liquid spreading (Al-Dahhan & Dudukovic, 1995). In accordance with this, a higher total liquid saturation is registered at this higher u_G (Figure 32c). It is noted that an increased wetting efficiency as a result of increased gas flux was reported for this pre-wetting mode by Al-Dahhan & Dudukovic (1995), which certainly indicates better liquid spreading (although their saturation decreased with gas velocity). However, present results pertain to low pressure conditions (although the gas density is 1.1 kg/m^3).

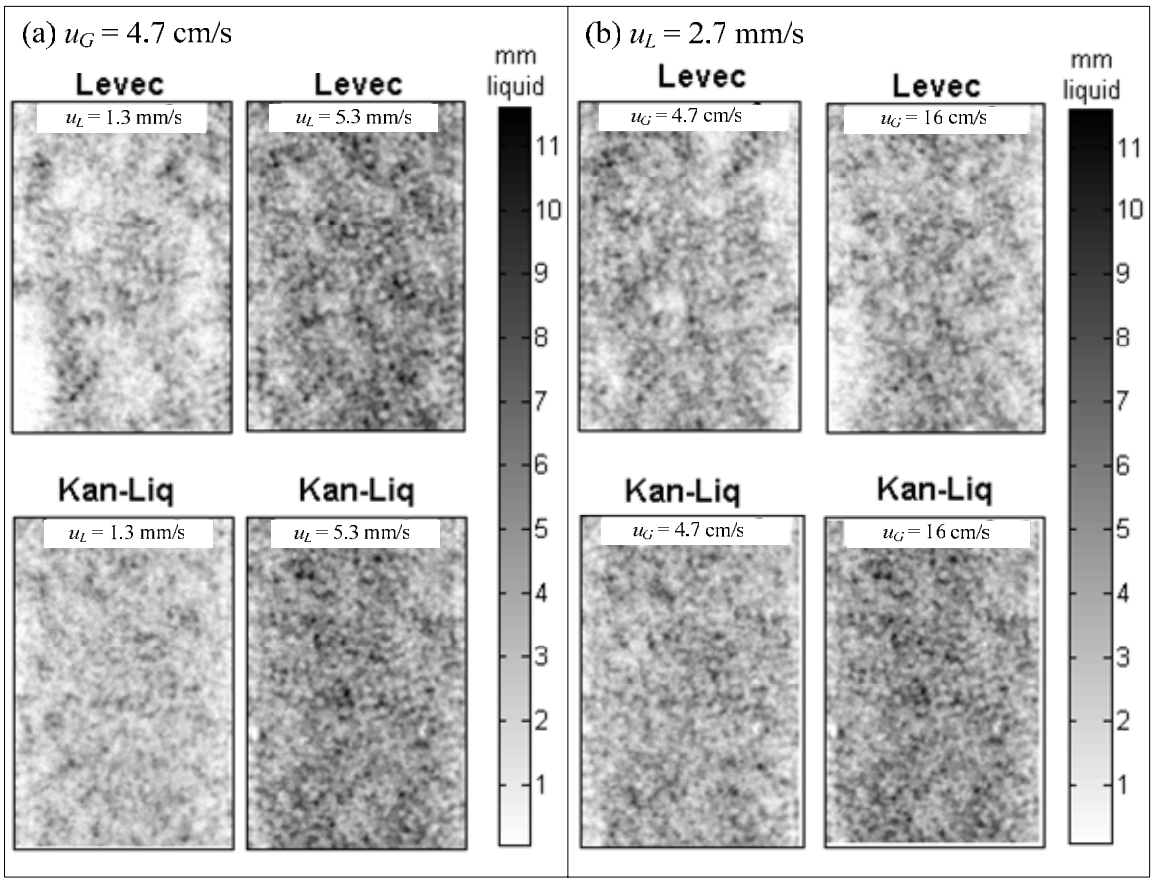

Figure 33. Flow patterns with increased fluid fluxes.

A mathematical analysis based on the calculation of maldistribution factors for these radiographic images is inappropriate. This is because all the information regarding the

liquid distribution transverse to the viewing plane is lost. The maldistribution factor would therefore be insensitive to changes in liquid morphology in that direction. In addition, due to the cylindrical column shape, a small change in the liquid morphology close to the wall (in the viewing plane) will drastically affect the factor, while even a substantial change to the flow morphology close to the centre of the column (in the viewing plane) will fail to affect it significantly. Maldistribution is therefore better investigated in quantitative terms by computed tomography.

Start-Up Dynamics

Little attention has been given to the time required (from start-up) for the liquid saturation to reach its steady state value (see Table 14). Ravindra et al. (1997b) reported that the time-to-steady-state (TSS) can vary from 10 to 360 minutes depending upon the start-up procedure, the nature of the packing and the inlet distribution. However, they only considered the Non-pre-wetted and Super pre-wetted modes of operation. Figure 34a shows the temporal evolution of liquid saturation as registered by both the gravimetric and radiographic techniques employed in this study. Note that both techniques register the same dynamic behaviour of the liquid saturation shortly after start-up in each mode. Also evident from Figure 34a is the fact that in these pre-wetting modes the saturation stabilized within 50-150 seconds. The Non-pre-wetted mode failed to reach steady state even after 4 hours of operation. Therefore Non-pre-wetted mode results are not reported elsewhere in this chapter. The differences in saturation for the different modes are in agreement with numerous studies on hydrodynamic hysteresis as summarized in Chapter 2 and extended in Chapter 4.

The rapidity of the saturation stabilization in the Levec, Kan and Super modes is further illustrated in Figure 34b. It shows successive radiographs of Levec and Kan-Liquid pre-wetted beds. Based on these, it appears that the Levec bed reaches a stable configuration within 10 seconds after the first liquid appears in the field of view. The Kan-Liquid bed reaches its stable configuration approximately 70 seconds after the liquid flow rate was

reduced from its high value. The Super and Kan-Gas modes had similar dynamics to that of the Kan-Liquid mode and are not shown for the sake of brevity. These trends form part of the characteristic trends list and are revisited in Chapter 7.

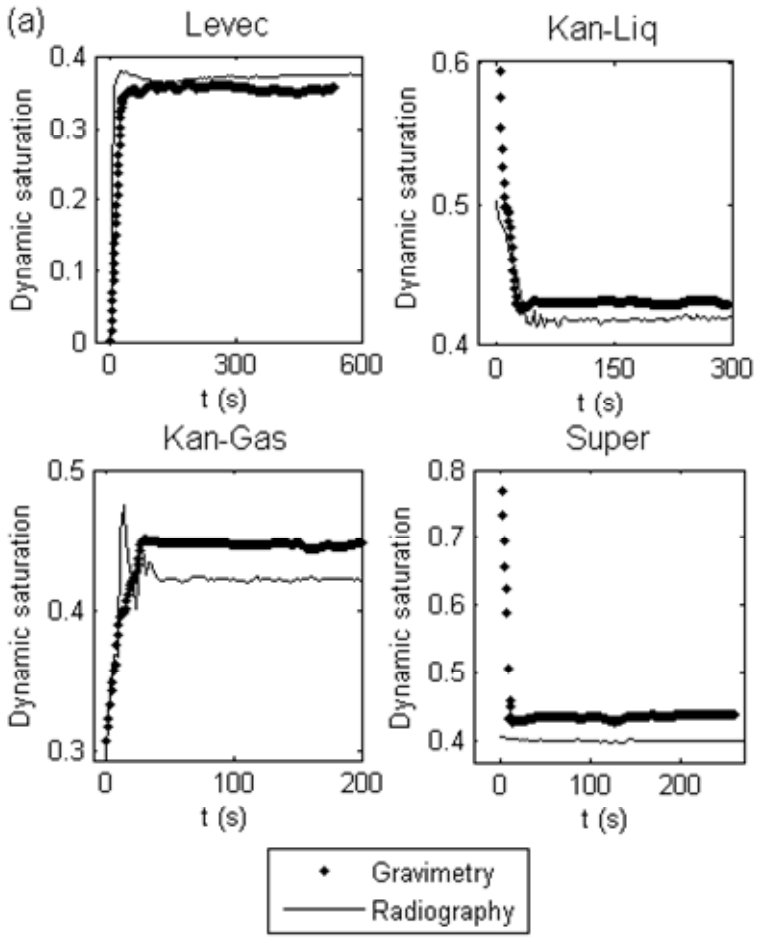

Figure 34a. Temporal saturation behaviour (saturation)

Temporal Stability at "Steady State"

The stability of the liquid configurations in the various pre-wetting modes over longer times can now be tested using the radiographic technique. Although the term steady state implies no change with time in any variable, it is interesting to investigate whether it is possible to have liquid path variations without necessarily changing the global parameter values.

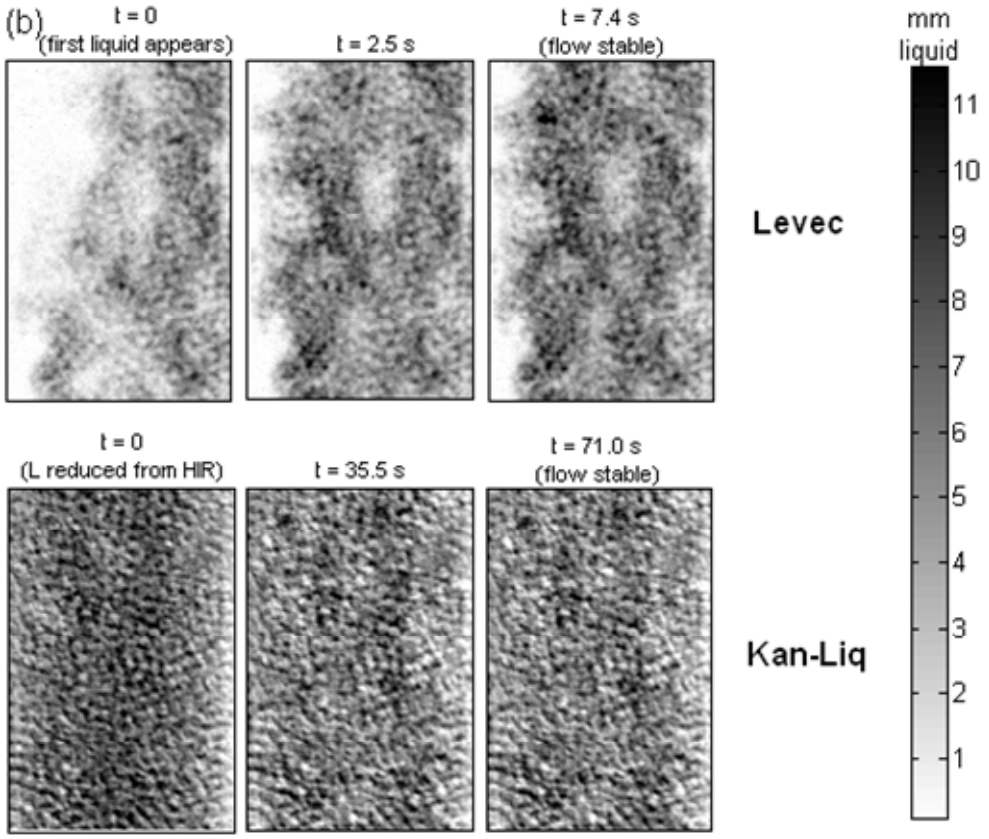

Figure 34b. Temporal saturation behaviour (images)

For each of the operating points, 200 consecutive radiographs approximately 2 seconds apart (spanning a total of 8 minutes of operation) were monitored for flow path changes. The 8 minutes were taken from a period where the bed-averaged liquid saturation showed no substantial change. In order to more clearly show local saturation changes, the first image is subtracted from the last - yielding a difference map (i.e. difference map = steady state image #200 – steady state image #1). These are shown in Figure 35. The dark areas in these images indicate locations where the saturation had a nett increase during the 8 minutes, while the light (white) areas indicate a nett decrease. Several millimetres (maximum of 3.4 mm) of change register at multiple locations in the Levec pre-wetted bed. Considering that there is a maximum of approximately 12 mm water at any given location (Figure 31) at these flow rates, this represents a large change in local saturation. Interestingly, there are almost no such saturation changes in the other pre-wetting modes.

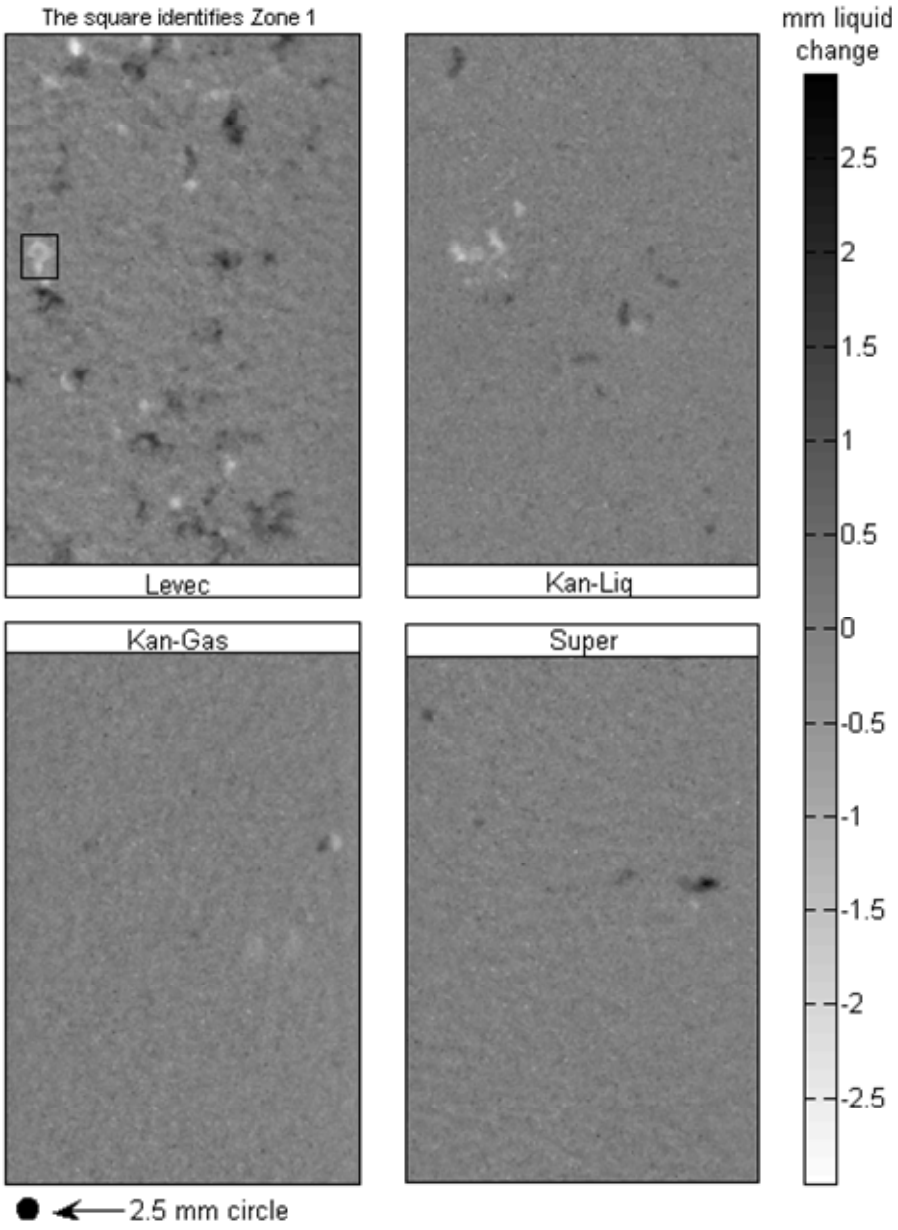

Figure 35. Difference maps (u_L = 8.0 mm/s, u_G = 1.6 cm/s)

Very similar difference maps are obtained at other liquid and gas flow rates (not shown). Additional characteristics of the saturation perturbations in the Levec mode are revealed by the difference maps. The length scale appears to be very close to one particle diameter (a single particle diameter is shown at the bottom of Figure 35 in direct proportion to the radiograph), although the shape is not spherical. There are both increases and decreases

in local saturation and these seem to cancel each other out so that the bed-average value remains nearly constant. In the Kan-Liquid, Kan-Gas and Super modes the flow pattern remains stable. The locations of temporal instability in the Levec mode are subsequently referred to as unstable zones. Having established the locations of these unstable zones, they can be monitored by examining consecutive radiographs (2 seconds apart) to establish when the liquid saturation change(s) occurred, how long such a change takes and whether it is a single change or multiple oscillations at that location. One way of illustrating this is to plot the total liquid thickness in an unstable zone against time. Figure 36a, zone 1, is such a plot for the unstable zone marked in Figure 35, clearly showing that there was one sudden de-saturation (at approximately 250 seconds). Figure 36 also includes such plots for other unstable zones (also at other gas and liquid fluxes). Zones are numbered consecutively for convenience. Their exact locations are not important apart from the fact that they were all present only in the Levec pre-wetted mode. In these plots, step changes indicate sudden increases or decreases in local saturation.

From all the timed data generated in this study, the following conclusions can be drawn:

- An increased saturation in one zone is sometimes (but not always) accompanied by a decreased saturation at another (close by). See for example Figure 36a zones 2 and 3 and Figure 36c zones 9 and 10. This suggests that the liquid had moved from one zone to the other.
- The change in saturation never takes longer than 5 seconds to complete (regardless of the flow velocities).
- The frequency of changes is very low (there are hundreds of seconds between changes).
- The same unstable zone sometimes experiences more than one saturation change (see zones 4 and 8 in Figure 36a and Figure 36c respectively). This suggests that there is some underlying aspect to the bed that can be associated with these saturation changes. However, at different flow rates it is not these same zones that undergo saturation changes (not shown).

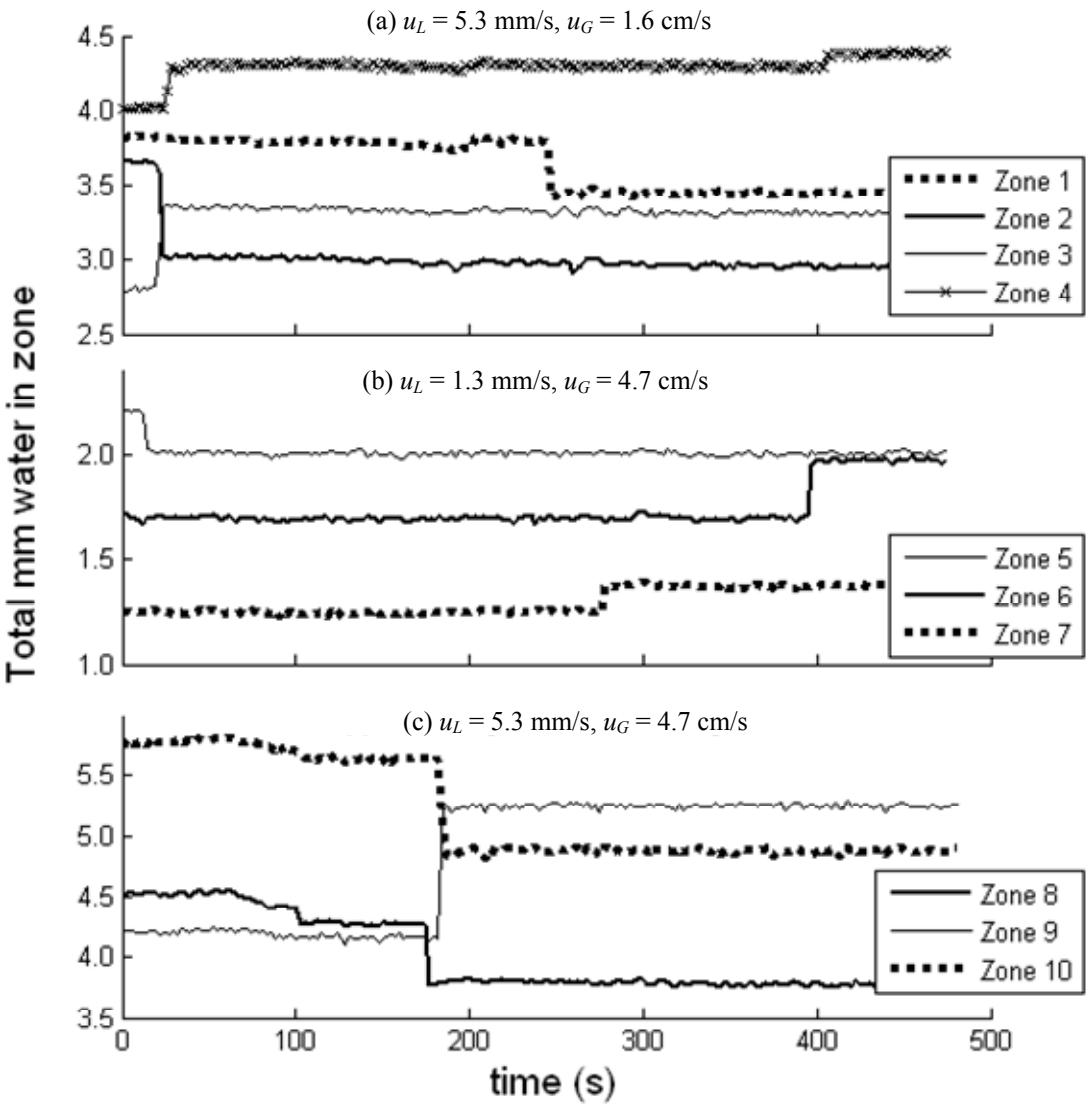

Figure 36. Liquid saturation changes in different zones showing the size and frequency of changes

- It cannot be concluded that either the frequencies of saturation changes or their magnitudes are linked to the liquid or gas flow rates.
- The local saturation changes in the Levec mode does not serve to increase the distribution uniformity and the flow pattern remains far removed from the Kan-Liquid mode (at least for the longest time under investigation here: 2.5 hours).

It is important to note that the difference maps employed here only shows the difference between the 200th and first images. As such, a difference map is incapable of registering saturation changes that cancel themselves out in the interval between the images used for its generation. That is, should a saturation increase somewhere in the bed be followed by a saturation decrease of the same magnitude within the 8 minutes it would not show on the difference map. However, such double (or multiple) changes do show on a standard deviation map which uses all of the images in the interval. These are calculated analogously to those of Anadon et al. (2005). Figure 37 shows a comparison between a difference map and a deviation map for the Levec pre-wetted mode shown in Figure 35. In every case presently under examination, the standard deviation maps and difference maps identified the same zones as unstable for the Levec mode.

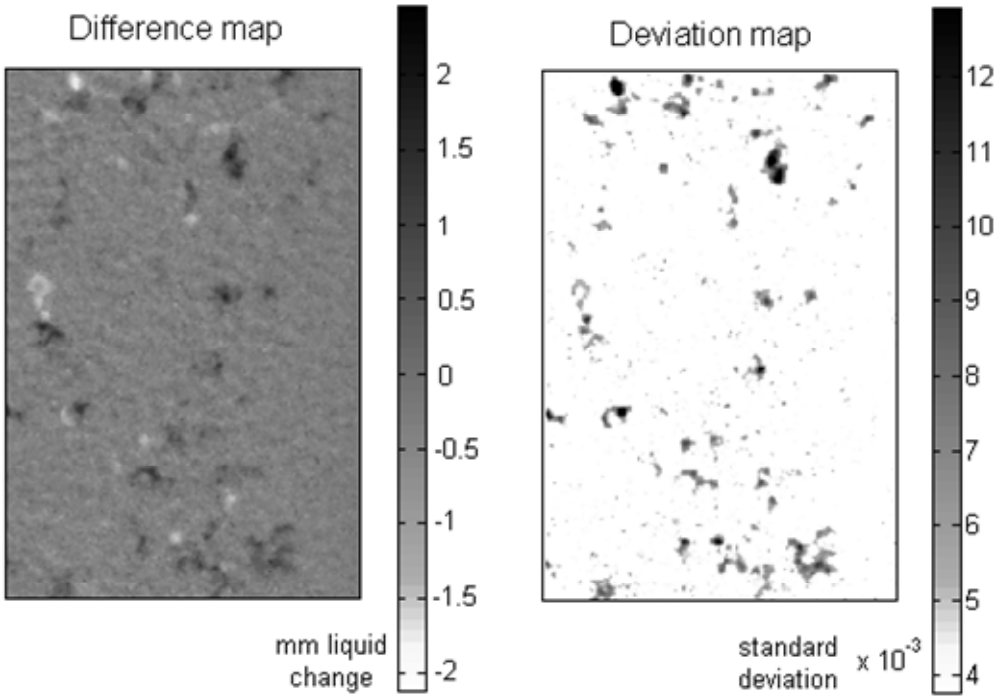

Figure 37. Comparison between a difference map and a deviation map (u_L = 8.0 mm/s, u_G = 1.6 cm/s)

This means that there where no zones that had double changes of opposing sign and equal amplitude in the time period under investigation. In the other modes both the difference and the deviation maps indicate no dynamic changes in flow pattern. Consequently, difference maps are preferred because they are capable of showing whether an increase or

a decrease in saturation had occurred while the standard deviation maps are not. It should be noted that the saturation changes reported here are not equivalent to those of Anadon et al. (2005). In their work, high frequency (several per second) localized saturation changes occurred in the Kan-Liquid mode close to the trickle-to-pulse flow transition boundary. It was shown how these instabilities are to be considered the precursors of the pulsing regime. In contrast, the low frequency instabilities reported in this study are inherent to the Levec mode in the trickle flow regime and occur at all velocities, but not in the Kan-Liquid, Kan-Gas and Super modes.

Saturation and Flow Pattern Reproducibility

For one set of gas and liquid flow rates, repeat runs for the Levec and Kan-Liquid modes were conducted. These two modes are the most commonly employed in literature. Figure 38a shows that in both pre-wetting modes the *total liquid saturation* had completely reproducible temporal behaviour with little difference between the steady state saturation values. However, close examination of the processed radiographs at steady state reveals that the liquid is not located at the same positions in the bed. This can be more clearly seen when the difference of two liquid saturation radiographs are taken (i.e. Run 1 radiograph – Run 2 radiograph) as shown in Figure 38b. Note that these runs were conducted directly after one another on exactly the same bed without moving it. Moreover, the same pre-wetting and operational procedures were followed. It is concluded that the *liquid morphology* is not exclusively determined by the bed structure and the pre-wetting method. However, both the total external saturation values and the general flow type are. This is true for both the Levec and Kan-Liquid pre-wetted beds, although it is more apparent for the former. Lutran et al. (1991) concluded that the flow pattern was reproducible given that the same pre-wetting procedure had been followed. However, examination of their figure 21 shows that although the general flow pattern was reproducible, the liquid was not located at exactly the same locations. It is therefore concluded that present results agree with those in Lutran et al. (1991).

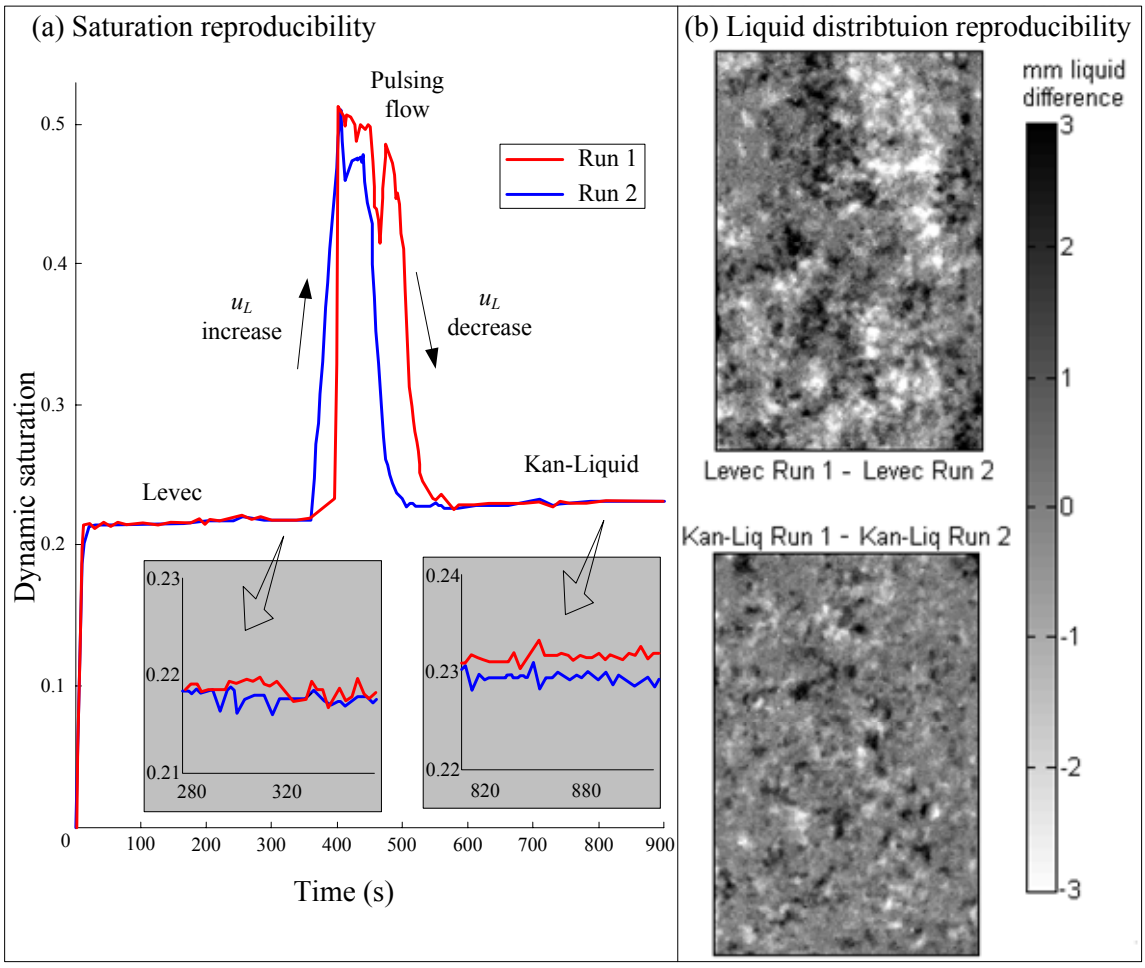

Figure 38. Flow pattern and liquid saturation reproducibility. (a) The overall saturation is reproducible (b) The flow pattern is not reproducible - dark and light intensities indicate areas where the saturation of runs 1 and 2 were different (u_L = 1.3 mm/s, u_G = 1.6 cm/s).

Radiography Conclusions

Radiographic imaging of trickle flow liquid saturation and distribution as a function of time, pre-wetting procedure and liquid and gas velocities is presented. A procedure to isolate the dynamic (free-draining) liquid from such images is introduced. The liquid saturation determined from these images is shown to agree with gravimetric liquid saturation measurements. This is encouraging since large diameter reactors are easier to radiograph than to weigh. The radiographic images indicate that the liquid saturation stabilizes shortly after the end of the start-up procedure for all pre-wetting modes except

non-pre-wetted beds. Present results agree with previous investigators in that Levec beds have lower saturations and are dominated by non-uniform flow. These flow non-uniformities persist at high liquid and gas flow rates. Although the bed-averaged liquid saturation and general flow type (sometimes referred to as rivulets for Levec pre-wetted beds and films for Kan and Super beds) are completely reproducible, the exact location of the liquid in the bed appears to have a stochastic nature. It has been established that there are local saturation changes (without changing the bed-averaged values) in the Levec mode, but not in the Kan-Liquid, Kan-Gas or Super modes. These changes are sudden but with a low frequency, occur at both high and low liquid and gas flow rates and do not appear to alter the general flow type. Apart from these *small, low frequency* perturbations in this one mode the overall flow structure remains stable for several hours, suggesting that the different modes of operation will prevail for long operating times. These observations form the basis of the computed tomography part of the radio-imaging study of trickle flow in the various pre-wetting modes, since the flow distributions obtained from the CT investigation will represent the actual (not time-averaged) flow patterns.

In summary, the capabilities of X-ray radiography (in particular its high temporal resolution) have been used to provide new insights into the stability and uniformity of trickle flow in several hydrodynamic states. This provides the basis for the detailed tomographic analysis of trickle flow multiplicity at the particle scale in the next section.

5.4.2 Three Dimensional Tomography Results

This section presents the preliminary results of the three dimensional tomographic investigation.

Tomography Reconstruction

Note that 2D radiographs of the bed (at steady state) were obtained for different rotations of the bed. A volume image (in three dimensions) can be reconstructed from the digitally recorded two dimensional radiographs by application of Beer-Lambert's law through the

Feldkamp-Davis-Kress (FDK) algorithm for cone beam reconstruction (details of which can be found in Feldkamp et al., 1984). Before applying the algorithm, a "white spot" filter is employed to remove individual pixels with exceedingly high intensity. In addition, a ring filter is employed to minimize reconstruction artefacts due to the rotation of the sample. The Octopus reconstruction package developed at the University of Ghent, Belgium, was used for this purpose (Dierick et al., 2004). A cross-section of the resultant volume image (trickle flow conditions) is shown in Figure 39.

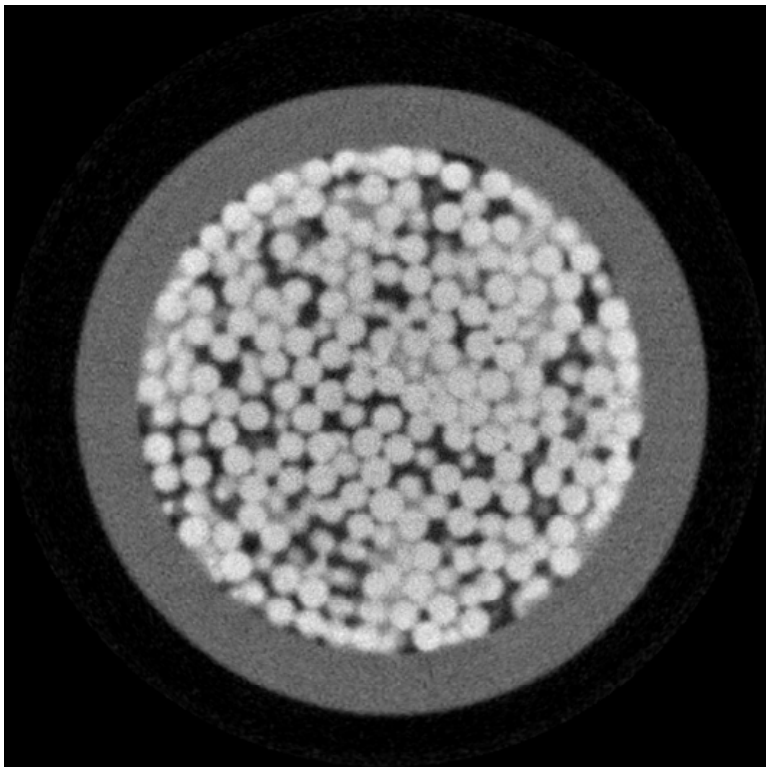

Figure 39. Cross-section of a raw reconstruction. Note the difficulty in clearly distinguishing the three phases.

It should be clear that it is very difficult to distinguish the three phases from this image. The reason for this is the presence of numerous "artefacts" in the image that are due to the following possible reconstruction errors (Boyer & Fanget, 2002):

- The *statistical error* in assuming a single photon energy as opposed to a distribution of energies (and the related phenomenon of beam hardening).

- Errors associated with the *accuracy of the acquisition instrumentation*.
- The *dynamic error* associated with phase instabilities during the image acquisition (i.e. if the local flow paths of the phases change with time).
- *Beam scattering* and *geometrical unsharpness* (because of the fact that the "point" source of the cone beam is in fact not an exact point) resulting in the inaccurate capturing of sharp phase distinctions (for example the solid-gas interface).

In fact, comparing various aspects of the radiography results (section 5.4.1) and the attributes of the raw reconstruction, estimates for some of these errors can be made:

- The dynamic error (flow path changes) is usually assumed to render the reconstructed image only valid in a time-averaged sense, i.e. as a representation of the flow patterns averaged over a period of time. However, the previous section has shown that trickle flow patterns are to be considered mostly stable (even the Levec mode flow pattern changes were small and of low frequency). This means that the dynamic error in the reconstructed images is small and that the patterns observed are stable flow configurations. This is the case only for the relatively low liquid velocities under investigation here, since the unstable nature of the flow pattern at high velocities is well known.
- By comparing the reconstructed image with the physical dimensions of the column and the particles, estimates for the geometrical and scattering effects can be made. Firstly, the inner diameter of the column (40 mm) spans 339 pixels, indicating that the spatial resolution is 118 μm/pixel. Examination of a single particle intensity profile through its centre (Figure 40), reveals that the geometrical unsharpness impacts approximately 4 pixels, i.e. 2 to each side of the interface. For comparison, the entire particle profile is approximately 20 pixels, i.e. one particle diameter is roughly captured by 20 pixels. Secondly, there is an apparent graininess to the inter-particle void space. This is a reconstruction artefact attributable to the scattering of X-rays that produces false signals from void space.

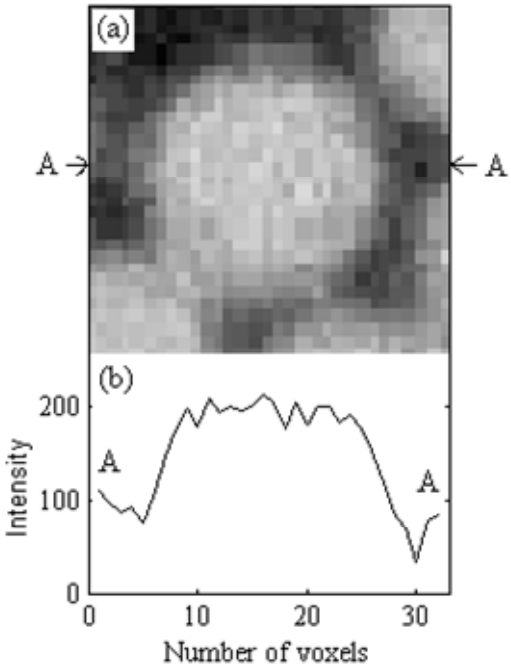

Figure 40. (a) Single particle reconstruction (cross-section). (b) Intensity line profile through section A-A showing the edge effect.

- Beam hardening is apparent in that the particles closer to the column wall have higher intensities than particles closer to the central axis (Figure 39). This is because the X-rays are initially absorbed (attenuated) non-linearly with material thickness. The beam hardening is reduced by the presence of the column wall which acts as a hardware filter (Basavaraj et al., 2005), although it was found to be very difficult to remove it entirely. Beam hardening is particularly undesirable because it makes the operation of thresholding ineffective (as discussed later).

Every effort was expended to tailor the FDK reconstruction algorithm to produce optimal reconstruction results for the system under investigation. These steps include the relatively thick wall to act as radiation (hardware) filter (Basavaraj et al., 2005), the optimal adjustment of the acquisition parameters (source-object distance, X-ray focal point, exposure time, number of rotations) and the reconstruction parameters (like the degrees of white spot and ring filtering). For example, the white spot filter compares each pixel value to the mean of its eight neighbours and sets the pixel value equal to this mean

only if the intensity exceeds the mean significantly, thereby preserving sharp edges (as compared to a regular median filter). Although the effectiveness of reconstruction algorithms has received some attention in recent years, there invariably remain some of the above mentioned inaccuracies in the final image. Some techniques are more prone to reconstruction errors than others. X-ray CT is particularly prone to beam hardening and scattering. As a result, some processing of the raw reconstruction is inevitable.

Image Processing According to the Thresholding Method

The objective of the processing steps is to obtain a ternary volume image where each spatial location in the bed is occupied by one of the liquid, solid or gas. Note that the reconstruction and processing steps are in fact not separate (a considerable deal of "image processing" has already gone into producing the raw reconstruction). Nevertheless, it is convenient to separate these operations conceptually, especially since the first has received considerable attention in literature and the second very little.

To start, consider that the usual way of identifying the three phases in an image like Figure 39, is to associate each phase with a range of intensities. This is done as follows:

1) The drained bed is thresholded at a value that yields a bed porosity equal to the independently measured bed-average value (0.41).
2) The drained bed image is then subtracted from the trickle flow image and this image is thresholded, yielding an image of the liquid only.
3) The result of step 2 is superimposed on the result of step 1, yielding the ternary gated image presented in Figure 41.

Clearly, the standard processing procedure fails to capture the detail of the bed structure and the flow pattern. An obvious way to see this is from examination of the particle contact points, where an artificial "neck" appears between the particles. This is understood in terms of the edge effect that results from the inaccurate capturing of particle edges (see Figure 40).

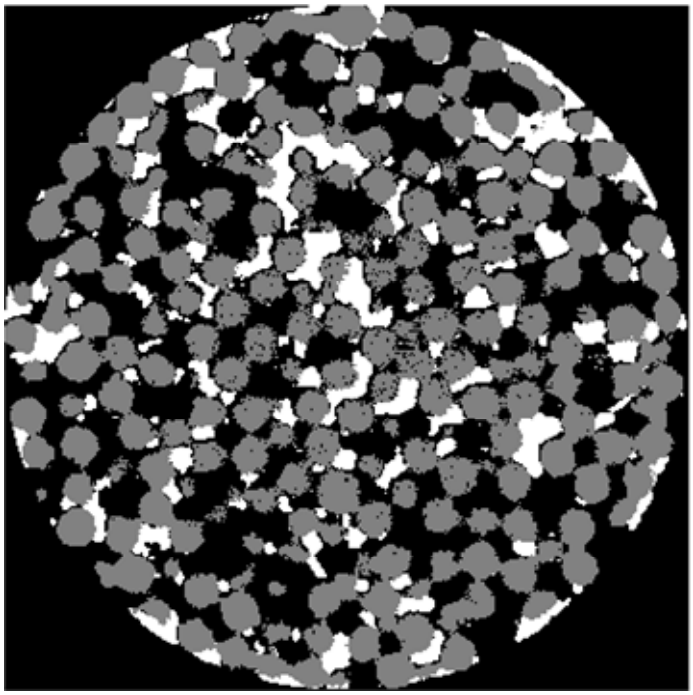

Figure 41. Ternary gated image processed according to the thresholding method

For illustrative purposes, it is shown schematically (in two dimensions) in Figure 42. For two nearly touching particles (Figure 42a), the reconstructed image will be similar to Figure 42b. The line profile through the contact point is shown directly next to each image. The thresholding procedure with the porosity target causes the particles to appear smaller than they are except for close to the contact point where additional phantom solid appears. Thresholding is seen to be poor at identifying edges when the intensity values on the outside of the particle differs from place to place (it is higher when there is another particle in close proximity). Liquid that is located close to particle contact points do not register on the ternary gated map generated by this procedure. Note also that this procedure is incapable of providing the bed porosity since its value has to be known in order to set the threshold level. Finally, thresholding is also very susceptible to beam hardening (which is why particles close to the centre of Figure 41 are only partially captured while excessive “necking” is observed close to the wall).

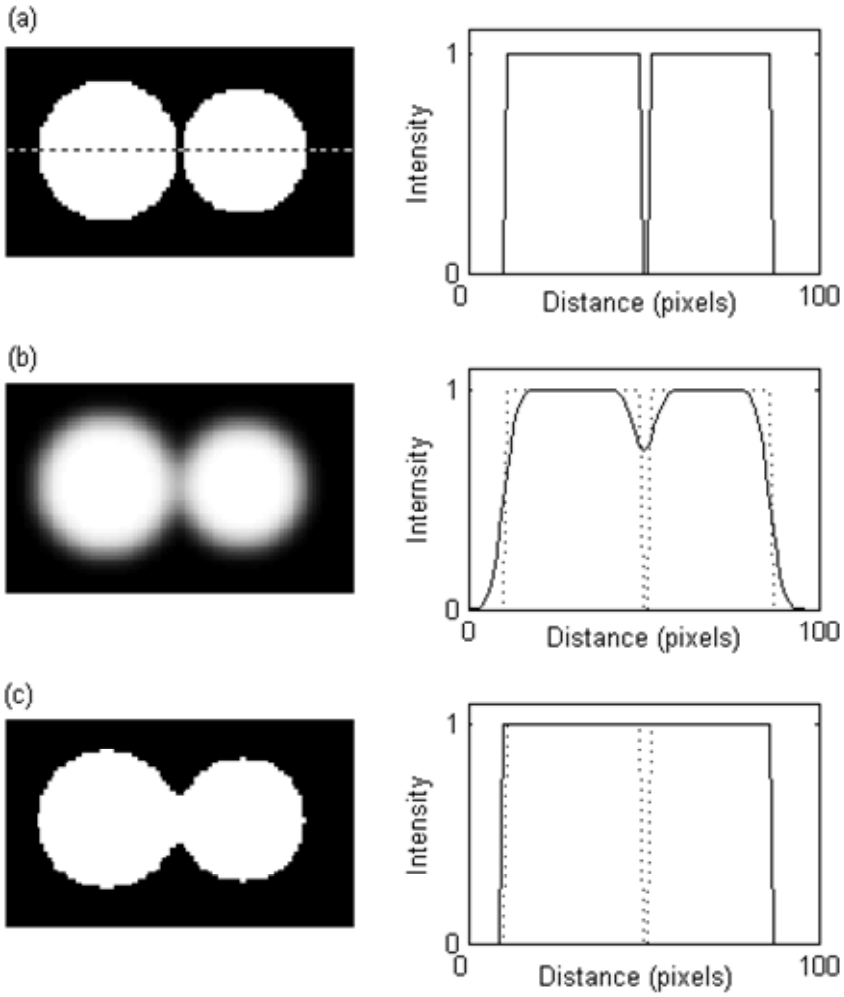

Figure 42. Schematic of how the edge effect creates "necks" when thresholding is used (a) true image (b) reconstructed image (c) thresholded reconstructed image.

As a first approximation, the radially averaged intensity, $\boldsymbol{I}_{avg}(r_c)$, can be corrected so that the average image intensity is the same at all distances from the central axis:

$$\boldsymbol{I}_{avg}(r_c) = \boldsymbol{I}_{avg}(r_c \to 0), \quad \text{where the subscript } avg \text{ refers to radial averages} \qquad (16)$$

However, this implicitly assumes that the local porosity is not a function of the distance from the central axis. Unfortunately, it is well established that the porosity decreases toward the wall (de Klerk, 2003). The peculiarities of a packed bed porosity distribution therefore make the beam hardening effect difficult to remove. Note that Figure 41 can be

used to once again investigate averaged properties of the flow. For example, it is possible to calculate a cross-sectional maldistribution factor by applying a form of equation 2 to the liquid in the image. One can then show that the Levec mode has a much larger maldistribution factor that any of the other pre-wetted modes and that the maldistribution factor decreases with velocity. However, these two important observations are clear from the images themselves (see Figure 50 in Chapter 6) without having to quantify them numerically (recall that the numerical value of the maldistribution factor has only relative significance). In fact, the radiographic images already showed these same trends (Figure 31). Figure 41 also provides a motivation for an improved image processing strategy because the particle scale phenomena cannot be obtained from this image. This includes interfacial areas and pore-scale statistics which will prove vital to the development of a multiplicity mechanism in Chapter 7.

5.5 Conclusions

This chapter introduced new experimental data on the localized behaviour of trickle flow in the various pre-wetted multiplicity modes. Using a 2D radiography technique, it was established that the trickle flow patterns are approximately stable over the longest period of time investigated (2 hours). This implies that CT visualizations yield the actual flow patterns and not time-averaged liquid distributions. Some of the hydrodynamic multiplicity trends already identified at the bed-scale were confirmed, while 2 major new trends were identified:

(Q) *Time to steady state*: the Kan-Liquid mode takes longer to reach a steady flow pattern than the Levec mode.

(R) There are *particle scale low frequency flow pattern changes* in the Levec mode, but not in any of the other pre-wetted modes.

In a second application of radio-imaging, 3D computed tomographic images of the different modes were produced and processed according to the usual method. The

resultant ternary image is inadequate to provide the necessary level of detail, and more advanced processing is required to establish the locations of the gas, liquid and solid in the bed. The development of such a processing strategy is the objective of the next chapter.